

TOPOLOGICAL MATTER

Fermi-arc diversity on surface terminations of the magnetic Weyl semimetal $\text{Co}_3\text{Sn}_2\text{S}_2$

Noam Morali^{1*}, Rajib Batabyal^{1*}, Pranab Kumar Nag^{1*}, Enke Liu^{2,3}, Qianan Xu², Yan Sun², Binghai Yan¹, Claudia Felser^{2,4,5}, Nurit Avraham¹, Haim Beidenkopf^{1†}

Bulk–surface correspondence in Weyl semimetals ensures the formation of topological “Fermi arc” surface bands whose existence is guaranteed by bulk Weyl nodes. By investigating three distinct surface terminations of the ferromagnetic semimetal $\text{Co}_3\text{Sn}_2\text{S}_2$, we verify spectroscopically its classification as a time-reversal symmetry-broken Weyl semimetal. We show that the distinct surface potentials imposed by three different terminations modify the Fermi-arc contour and Weyl node connectivity. On the tin (Sn) surface, we identify intra-Brillouin zone Weyl node connectivity of Fermi arcs, whereas on cobalt (Co) termination, the connectivity is across adjacent Brillouin zones. On the sulfur (S) surface, Fermi arcs overlap with nontopological bulk and surface states. We thus resolve both topologically protected and nonprotected electronic properties of a Weyl semimetal.

In topological semimetals, the dispersion of the topological surface bands is correlated with the topological bulk bands dispersion (1–8). Examples include Weyl and Dirac semimetals whose nontrivial topological properties arise from the existence of band-touching points, termed Weyl or Dirac nodes, in the electronic bulk band structure. Bulk Weyl nodes are formed under broken inversion or time-reversal symmetry. They exhibit definite chirality and are associated with open-contour “Fermi-arc” surface bands that emanate from one Weyl node and terminate at another with opposite chirality within the surface two-dimensional (2D) momentum space. Owing to this surface–bulk correspondence, the dispersion of the Fermi arcs reflects the Weyl cone band structure and particularly the bulk Weyl nodes energy. The Berry curvature associated with Weyl and Dirac nodes has been shown to result in a chiral anomaly in magnetotransport (9–11) and various nonlocal transport effects (12, 13).

The formation of Fermi arcs is guaranteed by the existence of bulk Weyl nodes and therefore provides a direct way to classify the bulk topology by means of surface probes. Nevertheless, some of the properties of Fermi arcs, such as their momentum-space contour and their connectivity among the Weyl nodes, are predetermined not by the bulk distribution of Weyl nodes but rather by the details of the surface termination (14, 15).

These properties, which can be controlled by surface manipulation, have direct implications for the magnetoelectric dynamics of the Weyl electrons that combine bulk and surface conduction, such as quantum oscillations (16, 17). Nevertheless, the level of susceptibility of the Fermi-arc bands to varying surface potentials has not been studied thoroughly in experiment.

Here, we study the compound $\text{Co}_3\text{Sn}_2\text{S}_2$ that was classified recently as a candidate time-reversal symmetry-broken Weyl semimetal (18, 19). In contrast to many material candidates (6, 20) and several experimental realizations (21–24) of the inversion symmetry-broken Weyl semimetals, time-reversal symmetry-broken Weyl semimetals were predicted in only a few magnetically ordered material candidates, including GdPtBi (25), $\text{Y}_2\text{Ir}_2\text{O}_7$ (1), HgCr_2Se_4 (26), and certain Co_2 -based Heusler compounds (27). In a few, including $\text{Co}_3\text{Sn}_2\text{S}_2$ (18, 28), a large anomalous Hall conductivity was reported (29), an indication of a magnetic Weyl phase; however, a spectroscopic verification remains challenging. In $\text{Co}_3\text{Sn}_2\text{S}_2$ (Fig. 1A), the magnetic properties arise from the kagome-lattice cobalt (Co) planes (30), whose magnetic moments order ferromagnetically out of plane below 175 K (18, 31). These Co planes are interleaved with buffer planes of triangularly ordered tin (Sn) and sulfur (S). Ab initio calculations (18, 19) find six Weyl nodes in the bulk Brillouin zone (BZ) (Fig. 1B). Their projection on the (001) surface identifies three Fermi-arc bands that connect the six surface-projected Weyl nodes. We show that the Fermi-arc connectivity in $\text{Co}_3\text{Sn}_2\text{S}_2$ varies with the surface termination, which also affects the intricate Weyl semimetal magnetoelectric response (Fig. 1C).

We use scanning tunneling spectroscopy to visualize the Fermi-arcs and to investigate their structure and connectivity in $\text{Co}_3\text{Sn}_2\text{S}_2$. The layered

structure of the material enabled us to study spectroscopically all three terminations of the (001) surface. Single crystals of $\text{Co}_3\text{Sn}_2\text{S}_2$ were cold cleaved at 80 K under ultrahigh-vacuum conditions and measured at 4.2 K in a commercial scanning tunneling microscope (STM) (UNISOKU). Energetically, the most favorable cleave plane is between the Sn and the S atomic layers (Fig. 1A). Indeed, most of the cleaved surface exhibits a triangular atomic structure, indicative of the Sn or S terminations, shown in Fig. 1, D and E, respectively. Rarely, we detect the less probable Co termination, indicated by the characteristic Kagome crystal structure as shown in Fig. 1F (for detailed element determination of termination scheme, see figs. S1 and S2). Each termination imposes a distinct surface potential that results in a distinct surface band structure. This diversity is captured by the characteristic dI/dV spectra that we find on the Sn-, S-, and Co-terminated surfaces, shown in Fig. 1, G to I, respectively.

We have performed ab initio calculations (see materials and methods) of the surface band structure of the three different terminations (19). We find that the three different terminations of the (001) surface in $\text{Co}_3\text{Sn}_2\text{S}_2$ exhibit not only distinct Fermi-arc contours, but also distinct connectivities of the (001) surface-projected Weyl nodes. On the Sn termination, the Fermi arcs connect Weyl nodes within the same BZ (Fig. 1J), whereas on the S termination, the connectivity is ambiguized by hybridization with nontopological surface-projected bulk bands (Fig. 1K), and on the Co termination the connectivity is across adjacent BZs (Fig. 1L). To demonstrate the marked influence that diverse connectivity may have on the electronic transport of Weyl semimetals, we consider, in Fig. 1C, a sample with distinct top and bottom terminations with different connectivity. In such a case, the semiclassical trajectory of the electrons under a weak perpendicular magnetic field would involve traversing all six Fermi arcs on either surface and crossing the bulk six times in between, before returning to the initial state. This stands in sharp contrast to the previously considered case of surfaces with identical connectivity, in which the electrons oscillate only through a single Fermi arc on each of the two surfaces (16, 17). Boundaries between surfaces with different Fermi-arc connectivity should also be further investigated because the change in connectivity across them may potentially invoke new 1D topological states.

To visualize the Fermi arcs and explore their energy evolution on the various surface terminations, we carried out measurements of the quasiparticle interference (QPI) patterns that elastically scattered electrons embed in the local density of states (LDOS) measured in differential conductance (dI/dV) maps (32, 33). A topographic image of the Sn-terminated surface decorated by moderate concentration of adatoms is shown in Fig. 2A. The QPI patterns on the Sn surface appear as weak ripple modulations in the corresponding dI/dV map (Fig. 2B). Here, and throughout the manuscript, our dI/dV mappings are normalized by the concurrently measured conductance, $I(V)$.

¹Department of Condensed Matter Physics, Weizmann Institute of Science, Rehovot 7610001, Israel. ²Max Planck Institute for Chemical Physics of Solids, D-01187 Dresden, Germany. ³Institute of Physics, Chinese Academy of Sciences, Beijing 100190, China. ⁴John A. Paulson School of Engineering and Applied Sciences, Harvard University, Cambridge, MA 02138, USA. ⁵Department of Physics, Harvard University, Cambridge, MA 02138, USA.

*These authors contributed equally to this work.

†Corresponding author. Email: haim.beidenkopf@weizmann.ac.il

We trace these QPI patterns to originate from subsurface impurities that appear fainter in Fig. 2A. Fourier decomposition of the QPI patterns separates surface scattering processes according to their transferred momentum, q , between incoming and scattered electronic wave functions. In general, the resulting QPI patterns consist of a complicated mixture of scattering processes that involve both Fermi-arc states and nontopological surface states. The identification of the respective surface bands that generate the QPI patterns is achieved by detailed comparison with calculations of the joint density of states (JDOS), on the basis of ab initio modeling. Throughout the paper, we highlight those scattering processes that involve Fermi-arc bands (marked in pink). We account for both the momentum structure of those patterns, as well as their dispersion with energy. The Fermi energy (zero bias in STM) is set consistently for all surface terminations to lie 45 ± 10 meV above the neutrality point, on the basis of fitting their respective QPI patterns with the ab initio calculations. This positions the Weyl nodes at about 105 meV above the Fermi energy. All QPI patterns presented are symmetrized according to the C_3 symmetry of the crystal (unsymmetrized data are presented in fig. S3). The spin character of these bands is neglected because all the surface bands are found to be fairly spin polarized within the ferromagnetic

phase (fig. S4). The orbital character of the different surface bands was not found to limit scattering processes significantly and is therefore disregarded as well (fig. S5).

The QPI patterns on the Sn surface have particularly sharp polygonal shapes. Representative QPI maps taken at 7.5 meV and at -10 meV are shown in Fig. 2, C and D, respectively. The main QPI patterns at 7.5 meV (Fig. 2C) are the hexagonal-shape QPI around $q = 0$ and replicas of it centered on Bragg peaks. To associate these QPI patterns with particular scattering processes, we consider the calculated surface density of states DOS(k) of the Sn termination, plotted in Fig. 2E, along with a simplified diagram of it (left and right panels, respectively). We find that the observed hexagonal QPI pattern originates from scattering processes (pink and red arrows in Fig. 2E) between a buckled hexagonal electron pocket around Γ and the adjacent edges of buckled triangular electron pockets at the K and K' corners of the BZ (captured also in the JDOS calculation shown in fig. S6A). The edges of the triangular pockets around K are formed by the open-contour Fermi-arc bands, each of which connects a pair of Weyl cones within the BZ (note that away from the Weyl node energy, the Fermi arcs merge with the rims of the dispersing Weyl cone).

At a lower energy, an additional pattern appears in the QPI that further contributes to the

identification of the involved scattering processes. With decreasing energy, the hexagonal QPI patterns increase in size, and toward -10 meV additional straight lines appear in the QPI along Γ -M that connect the adjacent corners of the QPI hexagons (Fig. 2D). The resulting honeycomb QPI pattern signifies a pocket structure of higher symmetry. Indeed, we find that the additional connecting lines in the QPI pattern originate from quasinearest conditions, marked by the open pink arrow in Fig. 2F, brought about by approximate colinearity of edges of adjacent triangular pockets at K and K' (corresponding JDOS calculation in fig. S6B). These scattering processes necessarily involve Fermi-arc bands. The shape, size, and orientation of the connecting line QPI patterns indicate that the Fermi arcs involved in these scattering process connect between pairs of adjacent Weyl nodes within the BZ.

The full energy evolution of the QPI patterns that we find on the Sn surface is captured in the energy-momentum cut along the K- Γ -M direction (Fig. 2G). The most prominent dispersing line (solid pink arrow), which grows outwards from $q = 0$ with decreasing energy, corresponds to the growing hexagonal QPI patterns. As shown in Fig. 2E, the hexagonal QPI is determined by the scattering vector between the edges of the hexagonal and triangular electron pockets. Because upon decreasing energy all electron pockets shrink

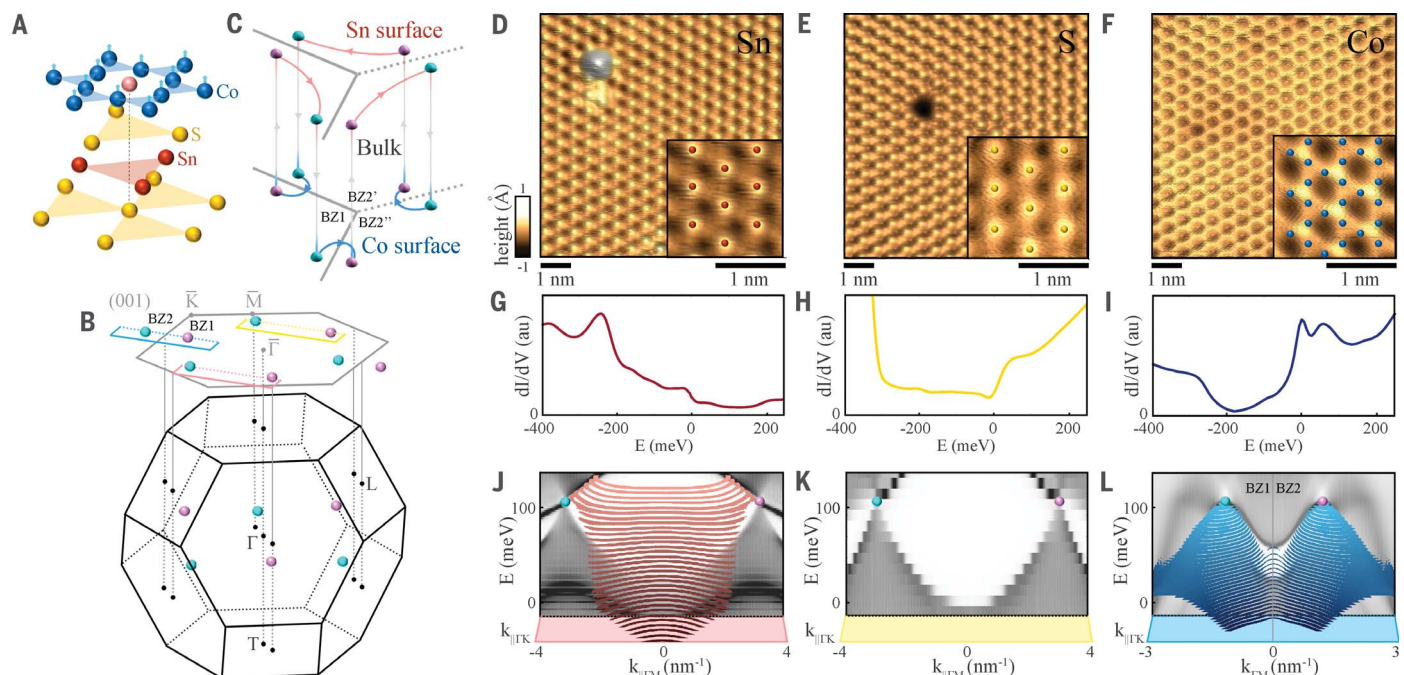


Fig. 1. Surface band structure on Sn, S, and Co terminations of $\text{Co}_3\text{Sn}_2\text{S}_2$. (A) The layered crystal structure with Co moments (arrows) ordered ferromagnetically. (B) Bulk BZ hosting three pairs of Weyl nodes and their (001) surface projection. (C) Illustration of Sn and Co surfaces with their respective intra- and inter-BZ Weyl node connectivity and the semiclassical electron magnetotransport trajectory (arrows). (D to F) Atomically resolved Sn, S, and Co surfaces, showing triangular, triangular, and kagome crystal structure, respectively. Insets show atomic lattice sites indicated by the

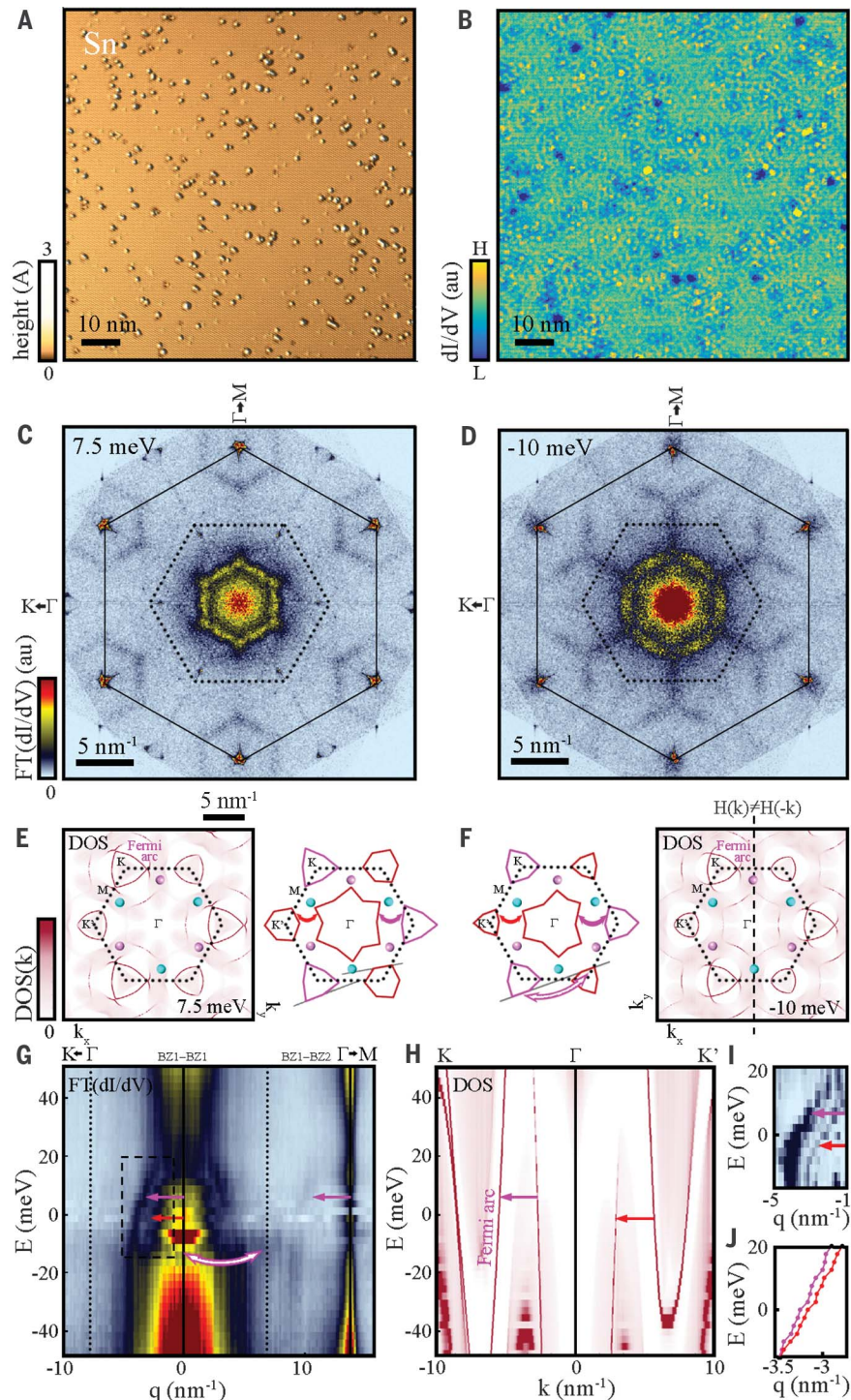
colored dots. (G to I) Typical dI/dV spectra on the different terminations. (J to L) Ab initio calculation of the band structure of $\text{Co}_3\text{Sn}_2\text{S}_2$ projected to Sn, S, and Co surface terminations. A cut through a pair of Weyl nodes [along a dotted line of the corresponding color in (B)] is given in grayscale, whereas the Fermi-arc dispersions [across rectangles in (B)] are marked in color. On Sn, the Fermi arcs connect Weyl nodes within the surface BZ, on S the connectivity is obscured by metallic surface bands, and on Co they connect Weyl nodes across adjacent BZs.

(Fig. 2H), the interpocket scattering vector, which generates the hexagonal QPI, grows. This evolution continues with decreasing energy, until at about -10 meV, an accidental symmetry between the K and K' pockets supports the quasinegating conditions and the onset of the connecting lines in QPI. These connecting lines are signified in Fig. 2G by the dark shaded area, along the Γ -M direction (open pink arrow), that connects the dispersing mode around $q = 0$ with its replica centered on the Bragg peak at $q = 13.5$ nm $^{-1}$.

Close inspection of the QPI patterns on the Sn surface allows us to observe direct signatures of time-reversal symmetry breaking, clearly manifested by the asymmetric calculated dispersion, $H(k) \neq H(-k)$ in Fig. 2, E and F. Accordingly, similar scattering processes on either side of the BZ should attain slightly different momentum transfer. Around zero bias, an inner scattering mode, which is fainter than the outer one (marked by red and pink arrows, respectively), appears in Fig. 2G along the Γ -K direction. It is hardly

visible because it overlaps with the central $q = 0$ broad peak that originates from inevitable long-wavelength inhomogeneities in the dI/dV map. To recover it, we make use of the isotropic nature of these inhomogeneities (see central disk shapes in Fig. 2, C and D), thus rendering the broad $q = 0$ peak symmetric along Γ -K and Γ -M. In Fig. 2I, we subtract the Γ -M QPI cut from the Γ -K one. This subtraction completely eliminates the $q = 0$ peak, which allows us to resolve two dispersing scattering modes (see additional information

Fig. 2. Intra-BZ Fermi-arc connectivity and time-reversal symmetry breaking on the Sn termination. (A) Topographic image of Sn-terminated (001) surface ($V_{\text{bias}} = 95$ meV, $I_{\text{set}} = 175$ pA) featuring adatoms and subsurface impurities. (B) dI/dV map taken on the region shown in (A), at $V_{\text{bias}} = 7.5$ meV [$V_{\text{AC}} = 2.1$ meV root mean square (RMS), $f = 733$ Hz], showing clear interference patterns. (C and D) Fourier transform of two dI/dV maps taken at different energies, showing sharp QPI patterns. Scattering within the BZ is contained within the dotted hexagon, and scattering among adjacent BZs within the solid hexagon, which connects the Bragg peaks. (E and F) Ab initio calculated DOS(k) and a corresponding simplified schematic pocket diagram. Important bands and scattering processes involving Fermi arcs (pink arrows) or surface-projected bands (red arrows). Lack of collinearity of the pocket edges in (E) and its existence in (F) are marked by gray lines. The collinearity gives rise to additional QPI patterns (open pink arrow). (G) Energy-momentum cut of the QPI along the K- Γ -M direction. Identified scattering processes are marked with corresponding arrows. (H) Energy-momentum cut of the calculated DOS(K) along K- Γ -K' capturing the energy evolution of the triangular electron pockets around K and K', the hexagonal electron pocket around Γ , and the scattering processes among them (arrows). (I) Two parallel Γ -K QPI modes [within the dashed box in (G)] highlighted by subtracting the corresponding Γ -M cut signifying time-reversal symmetry breaking. (J) Calculated dispersion of the momentum transfer from hexagonal to triangular pockets at K and K' (pink and red arrows, respectively).



in fig. S6, C to F). We naturally attribute the doubling of this QPI mode to the slight difference in momentum transfer when scattering from the hexagonal pocket at Γ to the triangular pockets at either K or K' (traced from ab initio calculations in Fig. 2J). The distinct extent in momentum space of the triangular pockets is a direct manifestation of broken time-reversal symmetry, and the appearance of the second inner QPI mode is a direct measure of it. These signatures of the time-reversal symmetry broken surface band structure and the Fermi arcs that it hosts on the Sn termination provide experimental confirmation for the existence of a magnetic Weyl semimetal phase in $\text{Co}_3\text{Sn}_2\text{S}_2$.

Having established Fermi-arc existence on the Sn termination, we now show that the Co-terminated surface exhibits a distinct configuration of Fermi arcs with different Weyl node connectivity. A topographic image of a Co-terminated surface and its corresponding dI/dV map are shown in Fig. 3, A and B, respectively. The associated QPI linecut taken along the high-symmetry line K- Γ -M (Fig. 3C) presents a rich QPI pattern with replicas that span up to the second-order Bragg peaks. The QPI pattern differs from the dispersion that we have presented on the Sn surface (Fig. 2G) owing to the distinct surface potential on the different crystal terminations. To resolve the main scattering processes, in particular the ones involving Fermi arcs, we

first identify the three main regimes in the energy evolution of the calculated band structure in Fig. 3D (further details are in fig. S7A): (i) At low energies we find six closed electron pockets around the BZ corners at K and K'; (ii) upon increasing the energy, all pockets widen until the three pockets around the K points, disconnect, and flatten, revealing the Fermi-arc connectivity. In contrast to the Weyl node connectivity observed on the Sn termination, where the Fermi arcs connect pairs of Weyl nodes within the same BZ, on the Co termination the Fermi arcs connect pairs of Weyl nodes from adjacent BZs. These changes in Fermi-arcs connectivity result from their hybridization with different sets of nontopological surface bands that coexist on the Co and Sn surface; (iii) upon further increase in energy, the surface pockets around K' split by hybridizing with the Fermi-arc bands around K, forming C-shaped bands that are partially composed of Fermi-arc states.

These three regimes of pocket structures correspond to three regimes that we identify in the evolution of the QPI patterns in Fig. 3C: (i) At low energies (-10 to 30 meV), we find several dispersing QPI patterns; (ii) at intermediate energies (30 to 60 meV), we find a single slightly dispersing mode; (iii) at high energies (60 to 80 meV), we find a single nondispersing mode. Identifying this energy evolution together with theoretical ab initio calculations of the JDOS allowed us to

resolve the scattering processes that give rise to the QPI patterns that are marked in dotted lines and arrows of the corresponding color in Fig. 3, C and D, respectively (see fig. S7 for further information). Among the scattering processes that we have identified, we concentrate here on those that involve Fermi-arc states (pink arrows), and bands that evolve with energy into Fermi arcs. The high-energy scattering between the C-shaped bands generates the nondispersing high-intensity peaks in QPI, as well as in the corresponding JDOS [ellipses in Fig. 3, E(iii) and F, respectively]. At intermediate energies, the Fermi-arc bands separate and give rise to the slightly dispersing scattering process marked by the pink arrow in Fig. 3D(ii). It generates the elongated QPI pattern demonstrated in Fig. 3E(ii) (pink ellipse) that accordingly signifies inter-Fermi-arc scattering. At low energies, we find multiple dispersing scattering processes whose corresponding origin and JDOS are shown in Fig. 3D(i) and G, respectively, and traced in the rich QPI patterns in Fig. 3H. The QPI patterns that we detect on the Co-terminated surface indeed differ substantially from those that we observed on the Sn termination. This allowed us to confirm the distinct surface band structure with distinct shape of Fermi arcs and Weyl nodes connectivity.

We conclude by discussing the S-terminated surface band structure, which presents a third distinct case. In contrast to gapped systems in

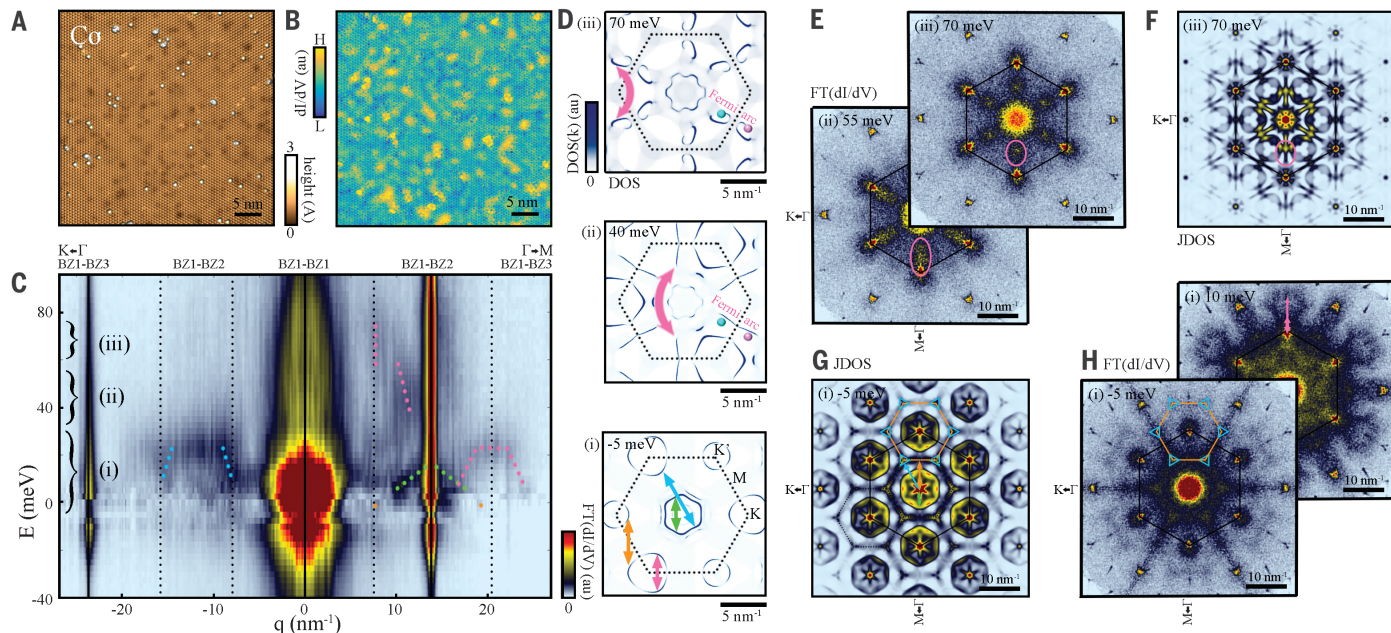


Fig. 3. Inter-BZ Fermi-arc connectivity on the Co surface. (A) Topographic image of Co-terminated (001) surface ($V_{\text{bias}} = -95$ meV, $I_{\text{set}} = 250$ pA) featuring adatoms and subsurface impurities. (B) dI/dV measurement taken on the region shown in (A), at $V_{\text{bias}} = -5$ meV ($V_{\text{AC}} = 2.1$ meV RMS, $f = 733$ Hz). (C) Energy-momentum cut of the QPI along the K- Γ -M direction. Dispersing scattering peaks are marked by dotted lines. Scattering events involving Fermi-arc bands appear in pink. Three energy QPI regimes (i to iii) are identified. (D) Calculated DOS(k) at different energies, representing the three regimes in the energy evolution of the band structure: (i) triangular pockets at K, K'; (ii) the pockets at K unfold

into Fermi arcs; (iii) Fermi arcs hybridize with triangular pockets at K'. Identified scattering processes are marked in colored arrows in correspondence with the colored dotted lines in (C). (E) Fourier transform of two dI/dV maps taken at intermediate (ii) and high (iii) energies, showing QPI broad peaks along Γ -M (marked by pink ellipses) that originate from the scattering processes in the respective energy ranges in (D). (F) Calculated JDOS at an energy corresponding to regime (iii). (G) Calculated JDOS at low energy. Identified scattering processes are marked by corresponding color in (D)(i). (H) Fourier transform of two dI/dV maps taken at relatively low energies, showing rich dispersing QPI patterns.

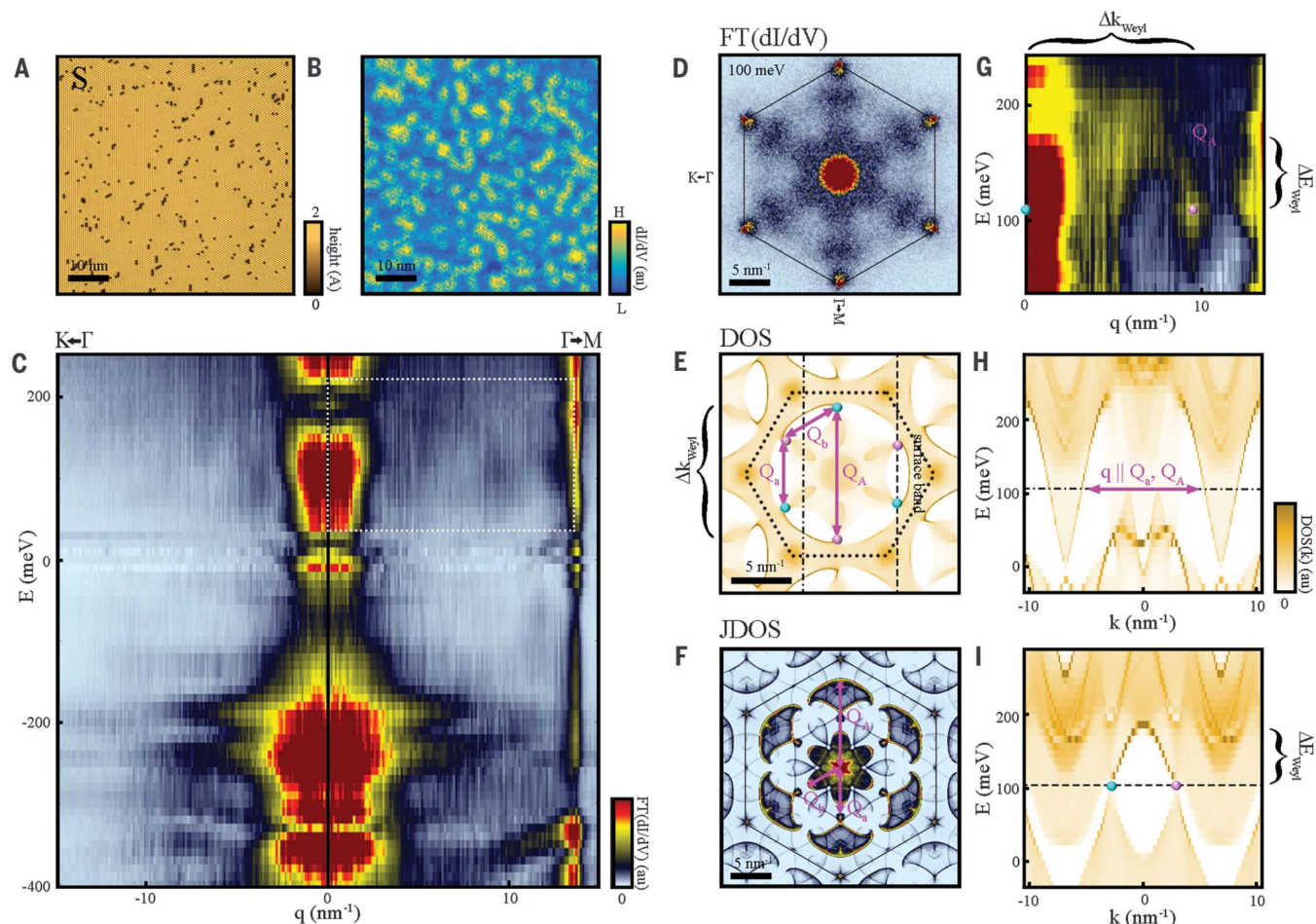


Fig. 4. Weyl cone dispersion on the S termination. (A) Topographic image of the S-terminated (001) surface ($V_{\text{bias}} = 50 \text{ meV}$, $I_{\text{set}} = 250 \text{ pA}$) featuring S vacancies. (B) dI/dV map taken on the region shown in (A) ($V_{\text{bias}} = 100 \text{ meV}$, $V_{\text{AC}} = 5.3 \text{ meV RMS}$, $f = 733 \text{ Hz}$), showing electronic interference patterns correlated with the location of the vacancies. (C) Energy-momentum QPI cut along the $K\rightarrow\Gamma\rightarrow M$ direction, showing several dispersing QPI branches. (D) Fourier-transformed dI/dV map at the vicinity of the Weyl node energy, showing the flower-shaped QPI pattern around Γ and broad peaks along $\Gamma\rightarrow M$. (E) Ab initio calculated $DOS(k)$ at the corresponding energy, showing a single sharp surface band and the extremal scattering

wave vectors ($Q_{a,b}$) among it, where Q_A corresponds to the largest momentum separation of the Weyl nodes, Δk_{Weyl} . (F) Calculated JDOS at the corresponding energy agrees well with the measured QPI pattern in (D). (G) Highlighted QPI cut [from the dotted rectangle in (C)] showing inward dispersing peak from which we extract the Weyl cones structure in momentum, Δk_{Weyl} , and energy, ΔE_{Weyl} . (H) Energy-momentum cut of the $DOS(k)$ along the dashed-dotted line in (E), showing the evolution of the $Q_{a,A}$ scattering processes. (I) Energy-momentum cut of the $DOS(k)$ along the dashed line in (E), showing the extent of the inter-Weyl cone bulk, ΔE_{Weyl} , gap as projected to the S surface termination.

which the topological surface states are protected by the bulk gap, the protection of the surface Fermi arcs is more subtle. To be protected from scattering into the bulk, the contour of the Fermi arcs should lie within the Weyl cone's bulk gap. The local surface potential, however, can push the Fermi-arcs contour out of that gap and hence lift their protection from scattering into the bulk. This is the case for the S-terminated surface for which the Fermi arcs overlap with surface-projected bulk bands at almost all energies and momenta away from the Weyl node energy (19). Nevertheless, the S-terminated surface, whose topographic landscape is dominated by vacancies (Fig. 4A), exhibits clear signatures of electronic interference in the dI/dV mappings (Fig. 4B).

The energy dispersion of the QPI pattern on the S-terminated surface along the $K\rightarrow\Gamma\rightarrow M$ sym-

metry line is shown in Fig. 4C. We find several dispersing patterns (shown in detail in fig. S8); however, here we focus our attention on the QPI features that appear along the $\Gamma\rightarrow M$ direction at $\sim 100 \text{ meV}$ (within the white dotted rectangle). In the Fourier-transformed dI/dV map taken at 100 meV (Fig. 4D), these QPI features correspond to the $\Gamma\rightarrow M$ broad peaks, located between the Bragg peaks and the centered flower-like pattern. In the calculated $DOS(k)$, at the corresponding energy shown in Fig. 4, E and H, we identify a single dominant surface band that decorates the rims of the bulk band and terminates in the vicinity of the Weyl nodes. Detailed calculation shows that it indeed hybridizes with the Fermi-arc bands as they emanate from the Weyl nodes (19). The calculated JDOS (Fig. 4F) is similar to the measured QPI in Fig. 4D, showing both the broad

peaks and the flower-like patterns. This identifies the broad QPI peaks with interband scattering processes (bounded by Q_a and Q_A), and the flower-like pattern with intraband scattering processes (bounded by Q_b) of that surface band.

Following the energy evolution of the broad peak QPI pattern, highlighted in Fig. 4G, we find that it shifts toward smaller momentum transfers with increasing energy and seems to terminate below 200 meV . This dispersion is well captured by the $DOS(k)$ calculation in Fig. 4H, which shows that the surface band remains bound to the rims of the bulk band. Finally, cutting the dispersion $DOS(k)$ through two adjacent Weyl nodes, as shown in Fig. 4I, reveals that the projected bands that the surface state follows are the bulk Weyl cones that hybridize ΔE_{Weyl} above the Weyl node energy. The dispersion of the QPI

pattern in Fig. 4G accordingly embodies the dispersion of the Weyl cones. In particular, its vanishing slightly below 200 meV corresponds to the merging of the two adjacent bulk Weyl cones and the termination of the Weyl gap about $\Delta E_{\text{Weyl}} = 95$ meV above the Weyl node energy. The maximal momentum transfer of $Q_A = 9.5 \text{ nm}^{-1}$ at the Weyl node energy indicates that the Weyl node momentum separation, Δk_{Weyl} , is in agreement with our ab initio calculation (Fig. 4E). Although on the S termination the Fermi-arc contours are pushed out of this bulk gap and therefore could not be detected, on the Sn and Co terminations, they lie within this gap, which protects their hybridization and allows their detection.

By exposing three different surface terminations in $\text{Co}_3\text{Sn}_2\text{S}_2$, we draw a distinction between the conserved properties of this topology class, such as the energy and momentum of the Weyl nodes, and those that are sensitive to the details of the surface, as the Fermi-arc's dispersion and Weyl node connectivity. Our results characterize the time-reversal symmetry-broken Weyl phase of the semimetal $\text{Co}_3\text{Sn}_2\text{S}_2$ and demonstrate the unprotected aspects of topological semimetals. These may manifest in other measurements, such as modified magneto-electric paths in quantum oscillation experiments, and demonstrate the potential to manipulate and engineer those topological states by controlled surface perturbations.

REFERENCES AND NOTES

- X. Wan, A. M. Turner, A. Vishwanath, S. Y. Savrasov, *Phys. Rev. B Condens. Matter Mater. Phys.* **83**, 205101 (2011).
- A. A. Burkov, L. Balents, *Phys. Rev. Lett.* **107**, 127205 (2011).
- A. A. Burkov, M. D. Hook, L. Balents, *Phys. Rev. B Condens. Matter Mater. Phys.* **84**, 235126 (2011).
- S. M. Young et al., *Phys. Rev. Lett.* **108**, 140405 (2012).
- Z. Wang et al., *Phys. Rev. B Condens. Matter Mater. Phys.* **85**, 195320 (2012).
- H. Weng, C. Fang, Z. Fang, B. A. Bernevig, X. Dai, *Phys. Rev. X* **5**, 011029 (2015).
- R. Batabyal et al., *Sci. Adv.* **2**, e1600709 (2016).
- H. Inoue et al., *Science* **351**, 1184–1187 (2016).
- D. T. Son, B. Z. Spivak, *Phys. Rev. B Condens. Matter Mater. Phys.* **88**, 104412 (2013).
- X. Huang et al., *Phys. Rev. X* **5**, 031023 (2015).
- C.-L. Zhang et al., *Nat. Commun.* **7**, 10735 (2016).
- S. A. Parameswaran, T. Grover, D. A. Abanin, D. A. Pesin, A. Vishwanath, *Phys. Rev. X* **4**, 031035 (2014).
- Y. Baum, E. Berg, S. A. Parameswaran, A. Stern, *Phys. Rev. X* **5**, 041046 (2015).
- Y. Sun, S.-C. Wu, B. Yan, *Phys. Rev. B Condens. Matter Mater. Phys.* **92**, 115428 (2015).
- S. Souma et al., *Phys. Rev. B* **93**, 161112 (2016).
- A. C. Potter, I. Kimchi, A. Vishwanath, *Nat. Commun.* **5**, 5161 (2014).
- P. J. W. Moll et al., *Nature* **535**, 266–270 (2016).
- E. Liu et al., *Nat. Phys.* **14**, 1125–1131 (2018).
- Q. Xu et al., *Phys. Rev. B* **97**, 235416 (2018).
- Y. Sun, S.-C. Wu, M. N. Ali, C. Felser, B. Yan, *Phys. Rev. B Condens. Matter Mater. Phys.* **92**, 161107 (2015).
- L. X. Yang et al., *Nat. Phys.* **11**, 728–732 (2015).
- S.-Y. Xu et al., *Science* **349**, 613–617 (2015).
- B. Q. Lv et al., *Phys. Rev. X* **5**, 031013 (2015).
- H. Zheng et al., *Phys. Rev. Lett.* **119**, 196403 (2017).
- M. Hirschberger et al., *Nat. Mater.* **15**, 1161–1165 (2016).
- G. Xu, H. Weng, Z. Wang, X. Dai, Z. Fang, *Phys. Rev. Lett.* **107**, 186806 (2011).
- S. K. Kushwaha, Z. Wang, T. Kong, R. J. Cava, *J. Phys. Condens. Matter* **30**, 075701 (2018).
- L. Muechler, E. Liu, Q. Xu, C. Felser, Y. Sun, arXiv:1712.08115v2 [cond-mat.mes-hall] (2017).
- T. Suzuki et al., *Nat. Phys.* **12**, 1119–1123 (2016).
- J.-X. Yin et al., *Nature* **562**, 91–95 (2018).
- R. Weirich, I. Anusca, Z. Anorg. Allg. Chem. **632**, 1531–1537 (2006).
- M. F. Crommie, C. P. Lutz, D. M. Eigler, *Nature* **363**, 524–527 (1993).
- N. Avraham et al., *Adv. Mater.* **30**, e1707628 (2018).
- N. Morali et al., Replication Data for: Fermi-arc diversity on surface terminations of the magnetic Weyl semimetal $\text{Co}_3\text{Sn}_2\text{S}_2$, Harvard Dataverse, version 1 (2019). <https://doi.org/10.7910/DVN/GAJUXY>
- N. Morali et al., Replication Data for: Fermi-arc diversity on surface terminations of the magnetic Weyl semimetal $\text{Co}_3\text{Sn}_2\text{S}_2$, Harvard Dataverse, Zenodo, version 1 (2019). <https://doi.org/10.5281/zenodo.3359829>

ACKNOWLEDGMENTS

We acknowledge fruitful discussions with A. Bernevig and L. Muechler. **Funding:** H.B. acknowledges support from the United States-Israel Binational Science Foundation (BSF, grant no. 2016389), Helmsley Charitable Trust (grant no. 2018PG-ISL006), the European Research Council (ERC) under the European Union's Horizon 2020 research and innovation program (grant agreement no. 678702), and the German-Israeli Foundation (GIF, I-1364-303.7/2016); E.L. acknowledges the National Natural Science Foundation of China (no. 51722106) and National Key R&D Program of China (no. 2017YFA0206303); B.Y. acknowledges financial support from the Willner Family Leadership Institute for the Weizmann Institute of Science, the Benoziyo Endowment Fund for the Advancement of Science, Ruth and Herman Albert Scholars Program for New Scientists, the European Research Council (ERC) under the European Union's Horizon 2020 research and innovation program (grant agreement no. 815869), and the collaborative Max Planck Lab on "Topological Materials." C.F. acknowledges funding by The Würzburg-Dresden Cluster of Excellence on Complexity and Topology in Quantum Matter - ct.qmat (EXC 2147, project ID 39085490). **Author contributions:** N.M., R.B., and P.K.N. acquired the data, performed the analysis, and wrote the manuscript. E.L. grew and characterized the samples. Q.X., Y.S., and B.Y. calculated the ab initio model. C.F., N.A., and H.B. conceived the experiment and wrote the manuscript. **Competing interests:** The authors declare no competing interests. **Data and materials availability:** Data reported in this paper are archived online at Harvard Dataverse (34) and Zenodo (35).

SUPPLEMENTARY MATERIALS

science.sciencemag.org/content/365/6459/1286/suppl/DC1
Materials and Methods
Figs. S1 to S8
References (36–39)

30 August 2018; accepted 14 August 2019
10.1126/science.aav2334

Fermi-arc diversity on surface terminations of the magnetic Weyl semimetal $\text{Co}_3\text{Sn}_2\text{S}_2$

Noam Morali, Rajib Batabyal, Pranab Kumar Nag, Enke Liu, Qiunan Xu, Yan Sun, Binghai Yan, Claudia Felser, Nurit Avraham and Haim Beidenkopf

Science 365 (6459), 1286-1291.
DOI: 10.1126/science.aav2334

Magnetic Weyl semimetals

Weyl semimetals (WSMs)—materials that host exotic quasiparticles called Weyl fermions—must break either spatial inversion or time-reversal symmetry. A number of WSMs that break inversion symmetry have been identified, but showing unambiguously that a material is a time-reversal-breaking WSM is tricky. Three groups now provide spectroscopic evidence for this latter state in magnetic materials (see the Perspective by da Silva Neto). Belopolski *et al.* probed the material Co_2MnGa using angle-resolved photoemission spectroscopy, revealing exotic drumhead surface states. Using the same technique, Liu *et al.* studied the material $\text{Co}_3\text{Sn}_2\text{S}_2$, which was complemented by the scanning tunneling spectroscopy measurements of Morali *et al.* These magnetic WSM states provide an ideal setting for exotic transport effects.

Science, this issue p. 1278, p. 1282, p. 1286; see also p. 1248

ARTICLE TOOLS

<http://science.scienmag.org/content/365/6459/1286>

SUPPLEMENTARY MATERIALS

<http://science.scienmag.org/content/suppl/2019/09/18/365.6459.1286.DC1>

RELATED CONTENT

<http://science.scienmag.org/content/sci/365/6459/1248.full>
<http://science.scienmag.org/content/sci/365/6459/1278.full>
<http://science.scienmag.org/content/sci/365/6459/1282.full>

REFERENCES

This article cites 36 articles, 3 of which you can access for free
<http://science.scienmag.org/content/365/6459/1286#BIBL>

PERMISSIONS

<http://www.scienmag.org/help/reprints-and-permissions>

Use of this article is subject to the [Terms of Service](#)

Science (print ISSN 0036-8075; online ISSN 1095-9203) is published by the American Association for the Advancement of Science, 1200 New York Avenue NW, Washington, DC 20005. The title *Science* is a registered trademark of AAAS.

Copyright © 2019 The Authors, some rights reserved; exclusive licensee American Association for the Advancement of Science. No claim to original U.S. Government Works